Nano Research

ISSN 1998-0124 CN 11-5974/O4
https://doi.org/10.26599/NR.2026.94908746

Research Article

Oxygen vacancies regulation of In_2O_3 for enhancing microwave absorption by conduction and polarization loss balance

Boli Zeng[1,2,§], Haowen Xing[1,§], Yihao Fan[1], Jianfeng Wu[1,3], Feijie Ge[1](✉), Shuanmei Li[4], Baoliang Zhang[1,3](✉)

[1] School of Chemistry and Chemical Engineering, Northwestern Polytechnical University, Xi'an 710129, China

[2] Xi'an Key Laboratory of Functional Organic Porous Materials, Northwestern Polytechnical University, Xi'an 710072, China

[3] Shaanxi Engineering and Research Center for Functional Polymers on Adsorption and Separation, Sunresins New Materials Co. Ltd., Xi'an 710072, China

[4] Northwest Rubber & Plastics Research and Design Institute Co., Ltd., Xi'an 712023, China

[§] Boli Zeng and Haowen Xing contributed equally to this work.

Nano Res., **Just Accepted Manuscript** • https://doi.org/10.26599/NR.2026.94908746

https://www.sciopen.com/journal/1998-0124 on Apr. 17, 2026

Just Accepted

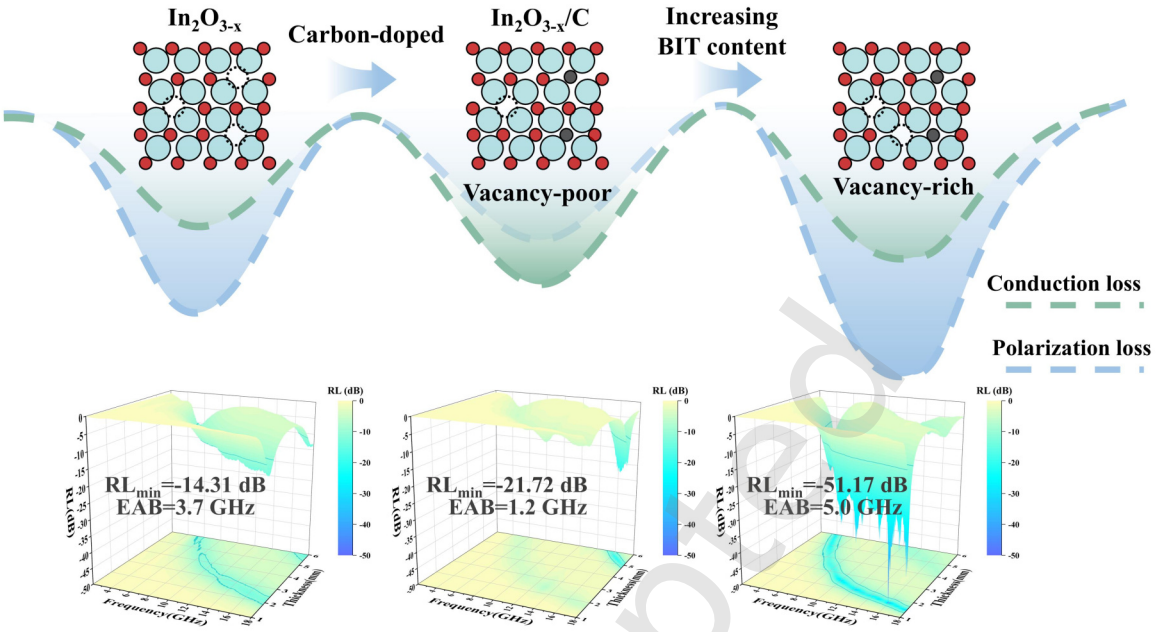

An effective absorption bandwidth of 5.0 GHz was achieved for In_2O_3 through the synergy of oxygen vacancy modulation and carbon doping.

Research Article

Oxygen vacancies regulation of In_2O_3 for enhancing microwave absorption by conduction and polarization loss balance

Boli Zeng[1,2,§], Haowen Xing[1,§], Yihao Fan[1], Jianfeng Wu[1,3], Feijie Ge[1,*], Shuanmei Li[4], Baoliang Zhang[1,3,*]

[1] School of Chemistry and Chemical Engineering, Northwestern Polytechnical University, Xi'an 710129, China

[2] Xi'an Key Laboratory of Functional Organic Porous Materials, Northwestern Polytechnical University, Xi'an 710072, China

[3] Shaanxi Engineering and Research Center for Functional Polymers on Adsorption and Separation, Sunresins New Materials Co. Ltd., Xi'an 710072, China

[4] Northwest Rubber & Plastics Research and Design Institute Co., Ltd., Xi'an 712023, China

[§] Boli Zeng and Haowen Xing contributed equally to this work.

Received: 24 February 2026; **Revised:** 1 April 2026; **Accepted:** 17 April 2026

Address correspondence to Feijie Ge, feijie.ge@nwpu.edu.cn; Baoliang Zhang, blzhang@nwpu.edu.cn

Cite this article: *Nano Research*, 2026, 19, 94908746 https://doi.org/10.26599/NR.2026.94908746

Abstract: As a transparent semiconductor, indium oxide (In_2O_3) exhibits intrinsically low dielectric parameter, rendering it ineffective for microwave absorption. Overcoming its inherent wide bandgap and limited dielectric loss to achieve effective microwave absorption presents a significant challenge. Herein, a lattice defect engineering strategy is proposed to construct oxygen vacancy-rich indium oxide (In_2O_{3-x}) and carbon-doped indium oxide (In_2O_{3-x}/C) particles with extrinsic defects. This approach achieves a breakthrough in the effective absorption bandwidth (EAB) of pristine In_2O_3, expanding it from 0 to 3.7 GHz. Furthermore, this study discovers that higher 1,2-benzisothiazoline-3-one dosages increase the oxygen vacancy concentration in In_2O_{3-x}/C, which is crucial for the material to exhibit microwave absorption capabilities. In particular, the In_2O_{3-x}/C-0.3 sample demonstrates enhanced microwave absorption through the synergistic effect of carbon doping, achieving a

* Corresponding author, Northwestern Polytechnical University, Youyi Road 127#, Xi'an (710072), China. Email: feijie.ge@nwpu.edu.cn (F. Ge), blzhang@nwpu.edu.cn (B. Zhang).

broad EAB of 5.0 GHz. Density Functional Theory calculations further reveal that the introduction of oxygen vacancies and carbon doping can optimize the band structure, reduce the bandgap and induce internal charge redistribution, thereby enhancing the conductive and polarization losses. This research is expected to open up a new avenue in the field of microwave absorption for In_2O_3 applications.

Keywords: Indium oxide, lattice defect engineering, oxygen vacancy, carbon doping, microwave absorption

1. Introduction

The advancement of microwave technology has greatly improved living standards, as evidenced by applications such as microwave ovens, radio communications and radar systems. However, the accompanying electromagnetic radiation pollution not only interferes with the normal operation of electronic devices, but also poses a significant threat to human health [1-4]. Electromagnetic wave (EMW) absorption materials are capable of converting incident electromagnetic energy into heat or other forms of energy, playing a critical role in suppressing electromagnetic interference and mitigating electromagnetic pollution. These materials demonstrate significant effects in enhancing electronic device stability, ensuring life safety, and advancing military radar stealth technologies [5-8]. Therefore, a wide variety of materials are designed and developed to meet the ever-increasing demand for EMW absorption. To improve the EMW attenuation capability of these materials, research strategies primarily focus on modulation in the mesoscopic level, including multi-component synergy [9-11], morphological innovation [12-14], and construction of heterogeneous interfaces [15, 16]. Although these approaches have improved the EMW absorption performance to some extent, there are still limitations in figuring out the effects of microscopic factors as well as in guidance for optimizing the material design.

In recent years, the development of defect engineering techniques, including atomic vacancies, ionic doping, and lattice distortion, has provided diverse strategies for controllable modulation of electromagnetic parameters in materials [17, 18]. Specifically, introducing

heterogenous elements into material lattices or generating point defects within them can produce corresponding impurity energy levels or defect energy levels in the band structure [19]. These modifications are conducive to enhancing the electrical conductivity, thereby improving the conduction loss capability of the material. Furthermore, the generation of point defects typically induces the formation of electric dipoles, which leads to corresponding polarization loss under external electromagnetic fields. For example, Liu at al. synthesized Se-doped CoS_2 and S-doped $CoSe_2$ with different doping levels by adjusting the S/Se mass ratio during annealing. It was revealed that the higher the vacancy concentrations and the richer the diversity of anion vacancy species, the more enhanced the absorption of EMW by the material [20]. Another study also confirmed that heteroatom doping can effectively increase the oxygen vacancy concentration, thereby enhancing the polarization loss capability of the material [21]. Zhang et al. introduced carbon vacancies into SiC through electron irradiation, which significantly enhanced the EMW absorption performance of the material [22]. In brief, employing defect engineering to modulate the intrinsic structures of materials can fundamentally optimize the electromagnetic parameters and further enhance the EMW absorption, proving as an effective strategy.

As an n-type transparent semiconductor, indium oxide (In_2O_3) is a promising candidate for EMW absorption material, although its inherent low dielectric parameter in the microwave frequency range makes it a significant challenge to achieve effective microwave absorption. Fortunately, extensive studies have identified oxygen vacancies in In_2O_3 lattices as shallow donors that enhance electrical conductivity [23, 24], providing a theoretical foundation for developing In_2O_3 as EMW absorption materials. Furthermore, computational studies reveal that oxygen vacancies bear lower formation energies under oxygen-deficient conditions [25], and this promotes the generation of oxygen vacancy defects in In_2O_3. Therefore, it is a feasible strategy to prepare In_2O_3 containing oxygen vacancies under a low oxygen partial pressure environment and investigate the correlation between oxygen vacancies and EMW absorption properties. To date, no such studies have been reported.

In this work, MIL-68(In) is employed as a precursor and subjected to stepwise annealing under oxygen-rich and vacuum conditions sequentially to obtain In_2O_3 and oxygen vacancy-rich indium oxide (In_2O_{3-x}). The role of oxygen vacancies in regulating the EMW

absorption performance of In_2O_3 is investigated through comparative analysis. To further enrich the defect density, a series of rod-shaped In_2O_{3-x}/C particles with extrinsic defects are constructed via doping carbon atoms into the In_2O_{3-x} material, using 1,2-benzisothiazolin-3-one (BIT) as an oxygen vacancy concentration modulator. The microwave absorption performance of the particles is optimized through coordinated effects. Meanwhile, a detailed analysis of the EMW dissipation mechanism is performed through density functional theory (DFT) calculations in combination with parameter measurements. This study demonstrates, for the first time, that defect engineering can enhance the microwave response of In_2O_3 as well as effectively expand the EAB. It also reveals the underlying microwave absorption mechanisms of In_2O_{3-x}, providing valuable insights for expanding its applications as a microwave-absorbing material.

2. Experimental Section

2.1. Materials

Indium nitrate hydrate ($In(NO_3)_3 \cdot xH_2O$), terephthalic acid (H_2BDC), 1,2-benzisothiazolin-3-one (BIT) were supplied by Adamas Reagents Inc., and N,N-dimethylformamide (DMF) was purchased from Guangdong Guanghua Sci-Tech Co., Ltd. All reagents were analytically pure and used directly without further treatment.

2.2. Synthesis of MIL-68(In)

The precursor MIL-68(In) was synthesized via a typical solvothermal method [26]. Specifically, 0.5 g of $In(NO_3)_3 \cdot xH_2O$ and 0.2 g of H_2BDC were dissolved in 70 mL DMF. The solution was transferred into a 100 mL Teflon-lined stainless-steel autoclave and reacted at 100 ℃ for 4 h. The resulting product was centrifuged, washed with ethanol, and vacuum-dried to obtain a white powder designated as MIL-0. Following this procedure, 0.1, 0.2 and 0.3 g of BIT were separately dissolved in DMF, with the corresponding products being labeled as MIL-0.1, MIL-0.2 and MIL-0.3.

2.3. Preparation of In_2O_{3-x}/C and In_2O_{3-x}

The as-prepared MIL-68(In) precursor was calcined in a tubular furnace under vacuum with a stepwise heating program. The heating rate was set at 5 ℃/min and maintained at

300 ℃ and 500 ℃ for 2 h, respectively. Based on the BIT dosage used in the synthesis of MIL-68(In), the resulting gray powders were sequentially labeled as In_2O_{3-x}/C-0, In_2O_{3-x}/C-0.1, In_2O_{3-x}/C-0.2, and In_2O_{3-x}/C-0.3. The as-synthesized MIL-68(In) precursor was calcined in a tubular furnace in air at 500 ℃ for 2 h with a heating rate of 5 ℃/min, yielding light yellow In_2O_3 powder. Subsequently, the In_2O_3 was annealed under vacuum at 500 ℃ for 2 h with identical heating rate to obtain In_2O_{3-x}.

2.4. Characterization

The morphology of the materials was observed using scanning electron microscope (SEM, FEI Verios G4). The internal structure and elemental distribution of the materials were characterized by transmission electron microscope (TEM, FEI TALOS-F200X) and energy-dispersive X-ray spectrometer (EDS). The composition content was calculated based on thermogravimetric analysis (TGA, Mettler Toledo Q50), with a temperature range of 30–700 ℃ and a heating rate of 5 ℃/min. The surface chemical structure of the samples was analyzed using X-ray Photoelectron Spectrometer (XPS, Kratos Axis Supra). The crystal structure of the samples was determined by X-ray Diffraction (XRD, Thermo Scientific 7000). The oxygen vacancy content of the samples was tested using an Electron Paramagnetic Resonance Spectrometer (EPR, Bruker A300). The conductivity of the samples was measured with an RST-11 type four-probe resistivity meter.

The electromagnetic parameters of the materials were measured using an Anritsu MS463222B vector network analyzer with a coaxial method. All samples were dispersed in a paraffin matrix at a filler loading of 45%. The electromagnetic wave absorption properties and reflection loss (*RL*) were calculated using Eqs. (1) and (2).

$$RL(dB) = 20\log\left|\frac{Z_{\text{in}}-Z_0}{Z_{in}+Z_0}\right| \quad (1)$$

$$Z_{in} = Z_0\sqrt{\frac{\mu_{\text{r}}}{\varepsilon_{\text{r}}}}\tanh\left(j\frac{2\pi f d}{c}\sqrt{\mu_{\text{r}}\varepsilon_{\text{r}}}\right) \quad (2)$$

where Z_{in}, Z_0, f, c, d, μ_r, and ε_r were input impedance of the material, impedance of free space, frequency of the electromagnetic wave, speed of light, thickness of the absorber, relative permeability, and relative permittivity, respectively.

2.5. DFT Calculations

The Perdew-Burke-Ernzerhof (PBE) functional combined with the projector-augmented wave (PAW) method was employed. A 2◊2◊2 k-point mesh sampling in the Brillouin zone was performed using the Monkhorst-Pack scheme. Van der Waals interactions were accounted for by the DFT-D3 method, while the strong Coulomb interactions between electrons were improved via the DFT+U approach. The plane-wave cutoff energy was set to 400 eV to ensure good convergence. All structures were fully relaxed until the residual force was less than 0.03 eV/Å, with an energy convergence tolerance of 10^{-5} eV per atom. On the basis of geometric optimization convergence, self-consistent field iterations were performed for each structure, followed by band structure calculations, density of state calculations, and differential charge analysis on the obtained wave functions. All these calculations were conducted using the Vienna Ab-initio Simulation Package (VASP) software [27].

3. Results and Discussion

3.1. Construction of Defective Indium Oxide

The preparation process of In_2O_3, In_2O_{3-x} and In_2O_{3-x}/C is schematically illustrated in Fig. 1. Indium nitrate hydrate ($In(NO_3)_3 \cdot xH_2O$), terephthalic acid (H_2BDC) and BIT were respectively used as the metal ion source, organic ligand, and modulator, to synthesize rod-shaped MIL-68(In) precursors through a typical solvothermal method (Fig. S1). The XRD patterns of MIL-68(In) shown in Fig. S2 are consistent with those reported in the literature [26, 28], confirming the successful synthesis of the MIL-68(In) precursor. Furthermore, with the introduction of BIT, no significant changes are observed in the diffraction peaks, indicating that the crystal structure remain unaffected by BIT. The precursor underwent annealing in air to yield In_2O_3, during which the organic components were oxidized and removed, while the metal coordination centers were oxidized to form the corresponding metal oxide (In_2O_3). Due to the minimal defects in In_2O_3 obtained through pyrolysis under oxygen-rich conditions, a subsequent annealing treatment was conducted under vacuum to increase the oxygen vacancy concentration in In_2O_3. The extremely low oxygen partial pressure under vacuum promoted the removal of lattice oxygen, thereby resulting in the formation of In_2O_{3-x}.

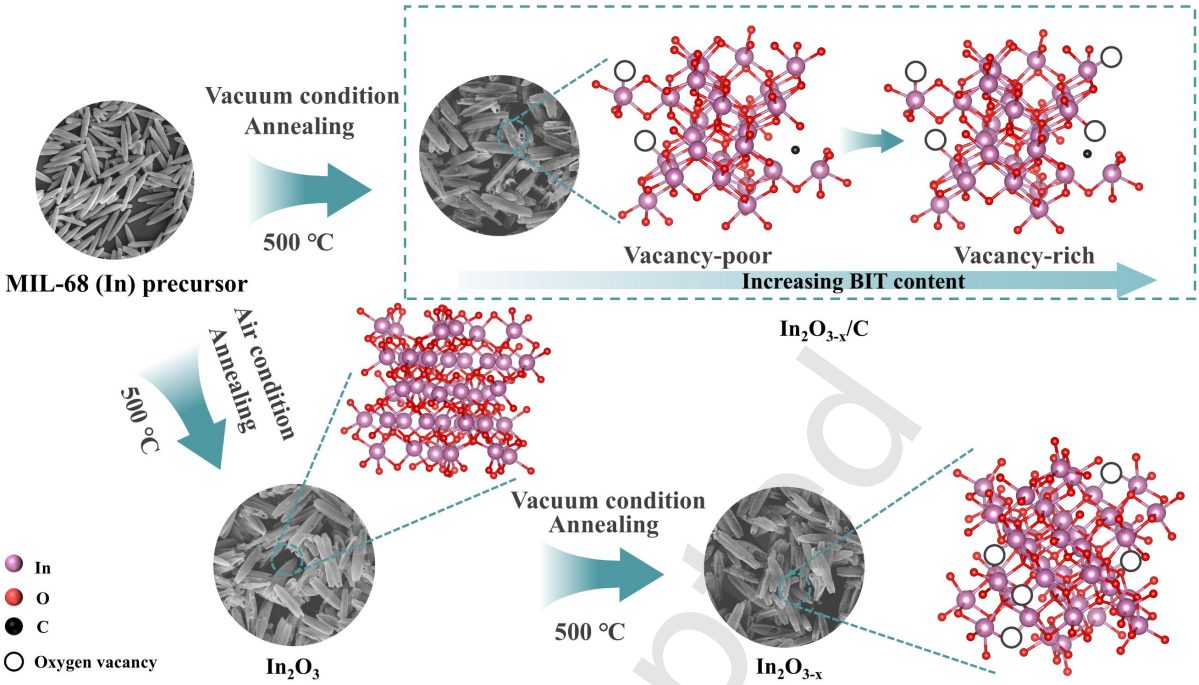

Figure 1 The schematic synthesis process of In_2O_3, In_2O_{3-x}, and In_2O_{3-x}/C.

To further increase the defects level of In_2O_{3-x} and enhance its corresponding dielectric loss capability, the precursor was directly annealed under vacuum. This treatment not only preserved the carbon components originating from the organic ligands but also promoted the formation of oxygen vacancies, ultimately yielding the In_2O_{3-x}/C. The morphologies of In_2O_3, In_2O_{3-x}, and In_2O_{3-x}/C are demonstrated in Fig. S3, where the annealed products exhibit varying degrees of structural contraction but retain their original morphology. It is worth mentioning that although the incorporation of BIT leads to some degree of morphological alteration, these subtle differences have negligible effects on the EMW absorption properties. More attention of this study is therefore paid to the influence of BIT on the formation of oxygen vacancies in In_2O_3. Previous studies have shown that the partial pressure of oxygen in the environment can influence the generation of oxygen vacancies in In_2O_3 [29]. Moreover, the thermal decomposition of organic matters (e.g., H_2BDC) in MIL-68(In) can generate oxygen ions [30], which in turn alter the local vacuum environment, thereby influencing the formation of oxygen vacancies. To ascertain the transition temperature of MIL-68(In) and the influence of BIT, in our study, TGA was applied on MIL-68(In) (Fig. 2(a)). The curves of all samples in the figure exhibit two stages of mass loss: I) the first stage lying between 100–200 ℃, during which the mass loss is attributed to the volatilization of organic matter

adsorbed on the material's surface and within its pores; II) the second stage occurring between 420–480 ℃, during which the mass loss results from the decomposition of indium-ion complexes to form In_2O_3, accompanied by the production of CO_2 and water vapor [28]. To completely convert MIL-68(In) into In_2O_3, the annealing temperature was set to 500 ℃. Moreover, with increasing BIT dosage, the mass loss in the first stage gradually decreases from 30.7% to 8.2%, indicating that BIT effectively reduces the adsorption of organic matter on the precursor, and this further weakens the impact of the thermal decomposition of the organic matter.

3.2. Characterization and Microwave Absorption Properties of In_2O_{3-x}

The In_2O_3 and In_2O_{3-x} samples were obtained through sequential two-step annealing under oxygen-rich and vacuum conditions, and their phases and structures were subsequently analyzed. As the XRD patterns show in Fig. 2(b), the diffraction peaks at 2θ = 21.49°, 30.58°, 35.47°, 51.04°and 60.68° correspond to the (211), (222), (400), and (622) planes of cubic In_2O_3 (PDF#06-0416) [31]. The oxygen vacancy concentrations in In_2O_3 and In_2O_{3-x} were determined through EPR testing, and the results are presented in Fig. 2(c). Compared to In_2O_3, In_2O_{3-x} exhibits a stronger signal intensity at g = 2.003, revealing a higher concentration of oxygen vacancy than that in In_2O_3. The O 1s peaks on the XPS spectra of In_2O_3 and In_2O_{3-x} reveal two peaks at 529.64 eV and 531.39 eV (Fig. 2(d)), corresponding to lattice oxygen and oxygen vacancy, respectively [32]. The area of the peak at 531.39 eV for In_2O_{3-x} is noticeably larger than that for In_2O_3. Additionally, the In 3d fine spectrum of In_2O_{3-x} (Fig. 2(e)) shows two peaks at 444.27 eV and 451.82 eV, assigned to In $3d_{5/2}$ and In $3d_{3/2}$, respectively [33]. These peaks shift by approximately 0.44 eV towards higher binding energies at 444.71 eV and 452.26 eV for In_2O_3, indicating that the In atoms in In_2O_{3-x} have a lower oxidation state. This is due to the formation of oxygen vacancies, which causes O^{2-} to transfer more lone pair electrons to the coordinatively unsaturated In^{3+}, thereby reducing its binding energy [34]. A detailed analysis of the microstructure and lattice information of In_2O_{3-x} was conducted using a double-spherical aberration-corrected TEM. The grain boundaries of In_2O_{3-x} are clearly observed in Fig. 2(f), and the polycrystalline structure is further confirmed by selected area electron diffraction (SAED) as shown in Fig. S4. Additionally, a large number of point defects

and distorted lattice fringes are identified in In_2O_{3-x} (Figs. 2(g) and 2(i)). The lattice fringes with a spacing of 0.29 nm correspond to the (222) plane of In_2O_3 (Fig. 2(h)).

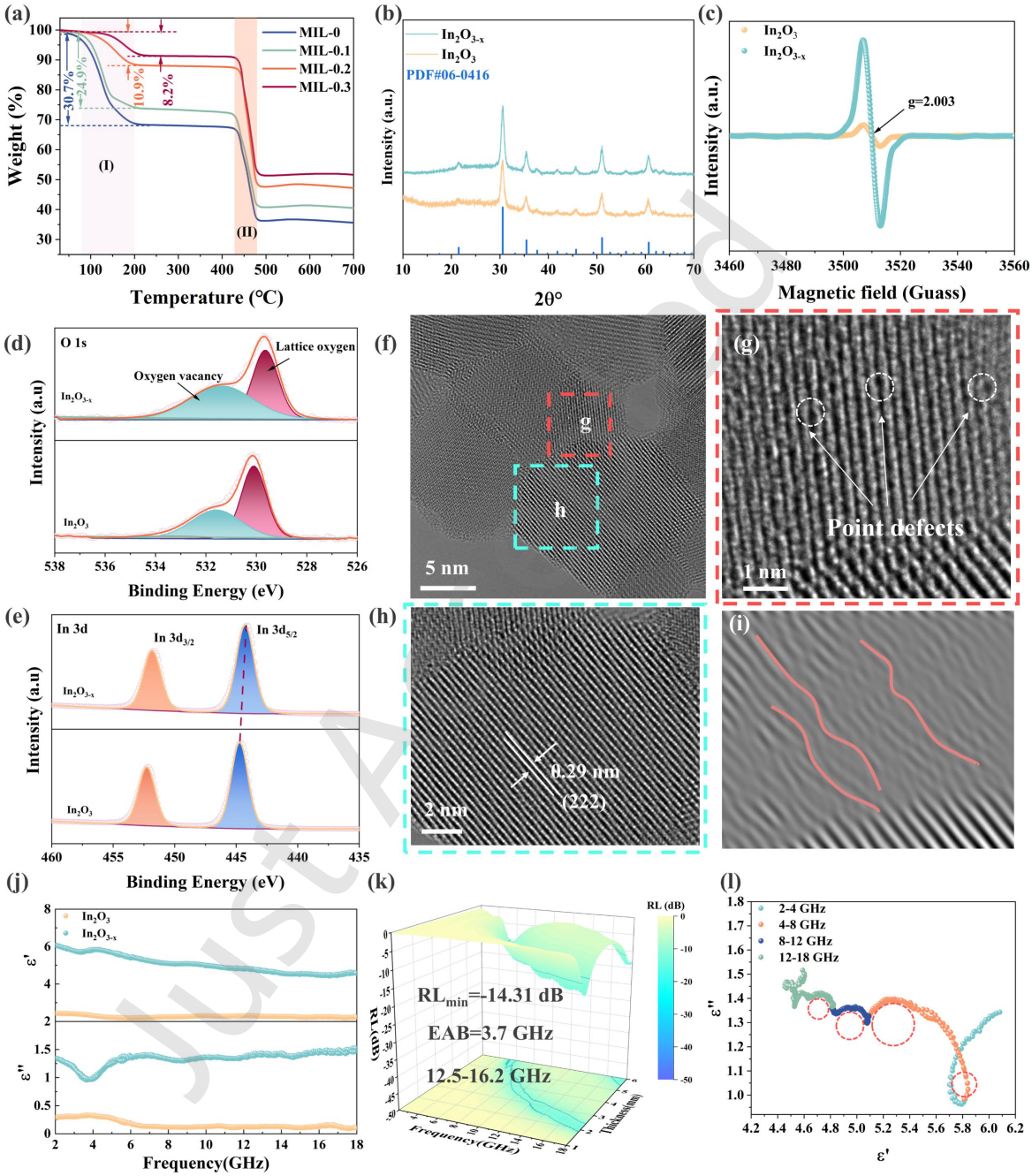

Figure 2 (a) TG curves of MIL-68(In). (b) XRD pattern. (c) EPR spectrum. (d) XPS spectra for O 1s and (e) In 3d. (f) HRTEM images of In_2O_{3-x}, (g) point defects, (h) lattice fringe, and (i) lattice distortion. (j) Real and imaginary parts of the complex permittivity of In_2O_3 and In_2O_{3-x}. (k) 3D *RL* and (l) Cole-Cole plot of In_2O_{3-x}.

The electromagnetic parameters of In_2O_3 and In_2O_{3-x} were measured to ascertain the influence of oxygen vacancies on the EMW absorption performance of In_2O_{3-x}. The real part

(ε') and imaginary part (ε'') of the complex permittivity for In_2O_3 and In_2O_{3-x} are presented in Fig. 2(j). Typically, a higher ε' value indicates stronger electromagnetic energy storage capacity of the material, while a higher ε'' value corresponds to enhanced reflection loss (*RL*) capability. Compared with In_2O_3, In_2O_{3-x} exhibits higher ε'' and ε' values, indicating its enhanced capability for EMW attenuation. This is because oxygen vacancies can induce the formation of defect dipoles, resulting in dipole polarization, which leads to the enhancement of the dielectric permittivity of In_2O_3 [35, 36]. As shown by the 3D *RL* topographies in Figs. S5 and 2(k), In_2O_3 exhibits an EAB of 0 GHz at any matching thickness, whereas In_2O_{3-x} demonstrates a broad EAB of 3.7 GHz@2.7 mm (12.5–16.2 GHz). This result proves that oxygen vacancies can significantly enhance the microwave absorption properties of In_2O_3. The attenuation mechanism of EMWs for In_2O_{3-x} was analyzed using Cole-Cole curves [37]. According to the Debye theory, each semicircle in the curve corresponds to a polarization relaxation process [38]. Multiple distinct semicircles observed in Fig. 2(l) indicate that In_2O_{3-x} primarily relies on polarization effects to dissipate EMWs, and oxygen vacancies can serve as polarization centers to augment the polarization loss.

3.3. Physical Properties and Microwave Absorption Performance of In_2O_{3-x}/C

Although the presence of oxygen vacancies endows In_2O_{3-x} with microwave absorption properties, the single defect form results in suboptimal *RL* capability. To address this problem, carbon doping was applied to In_2O_{3-x} to enrich the extrinsic defects, giving rise to rod-shaped In_2O_{3-x}/C particles. The XRD peaks of these In_2O_{3-x}/C particles are consistent with that of cubic In_2O_3 (Fig. 3(a)). Additionally, a broad diffraction peak attributed to amorphous carbon is observed at approximately 25° [5]. Comparison of the XRD peaks for the products reveal a slight shift of the diffraction angle corresponding to the (211) crystal plane of both In_2O_{3-x}/C and In_2O_{3-x} towards higher angles (Fig. 3(b)). Correspondingly, the interplanar spacing is calculated to decrease according to the Bragg equation, which could be attributed to lattice contraction induced by oxygen vacancies. Fig. 3(c) shows the oxygen vacancy concentration of the samples, following the order: In_2O_{3-x}/C-0.3 > In_2O_{3-x}/C-0.2 > In_2O_{3-x}/C-0.1 > In_2O_{3-x}/C-0. This trend is consistent with that revealed by the O 1s XPS spectra of In_2O_{3-x}/C

(Fig. S6), indicating that the oxygen vacancy concentration in In_2O_{3-x}/C increases with increasing BIT dosage. The full XPS survey spectra of In_2O_{3-x}/C clearly present the characteristic peaks of In, O, and C (Fig. 3(d)). As further confirmed by the C 1s spectra (Fig. 3(e)), no characteristic peaks of S deriving from BIT are detected. Therefore, there is no S in In_2O_{3-x}/C, eliminating the influence of S on the EMW absorption process.

The morphology, structure, and crystalline features of the materials were analyzed by TEM. All the In_2O_{3-x}/C samples exhibit hollow structures with uniform carbon distribution (Figs. 3(f) and S7), and their surfaces are composed of In_2O_3 nanoparticles (Figs. 3(g) and 3(h)). This structural evolution originates from the annealing process, during which the organic components in MIL-68(In) thermally decompose into CO_2 and H_2O, while indium ions are in situ converted into In_2O_3, forming the hollow structures whose surfaces are composed of In_2O_3 nanoparticles. The surfaces and interiors of the In_2O_{3-x}/C-0, In_2O_{3-x}/C-0.1 and In_2O_{3-x}/C-0.2 materials exhibit distinct mass-thickness contrast variations (Fig. S7), resulting from inward contraction of the structure induced by the surface-to-interior temperature gradient during pyrolysis. On the other hand, point defects, distorted lattice fringes and the (222) plane of In_2O_3 are apparently observable in Figs. 3(i)–3(k), and the SAED pattern further confirms the polycrystalline structure of In_2O_{3-x}/C (Fig. 3(l)). Thermal stability of the In_2O_{3-x}/C materials evaluated by TGA reveal 54.7% and 48.5% mass loss under O_2 and N_2 atmospheres (Fig. S8), respectively, indicating that the carbon content in In_2O_{3-x}/C is approximately 6.2%. With increasing BIT dosage, the ε' and ε'' values of In_2O_{3-x}/C increase as well (Figs. 3(m) and 3(n)), surpassing those of In_2O_{3-x}. This result indicates that the incorporation of carbon atoms can further enhance the EMW energy storage and dissipation capabilities of In_2O_{3-x}. Moreover, the ε' and ε'' curves of In_2O_{3-x}/C evolve from flat to steep as the mass of BIT increases from 0 to 0.3 g, indicating enhanced polarization relaxation processes. This enhancement should be attributed to oxygen vacancies acting as polarization centers, which endows the material with improved polarization loss capability [20]. And the higher the oxygen vacancy concentration, the stronger the polarization loss capability. When it comes to the electrical conductivity, measurements show that the conductivity of In_2O_{3-x}/C also increases with increasement of the BIT dosage (Fig. 3(o)). This trend is attributed to the role of oxygen vacancies, which enhances the electrical conductivity

of In_2O_3 [23, 39]. The conduction loss (ε_c'') and polarization loss (ε_p'') of In_2O_{3-x}/C are calculated using Eq. (3), and the results are presented in Fig. 3(p).

$$\varepsilon'' = \varepsilon_p'' + \varepsilon_c'' = \frac{\varepsilon_s - \varepsilon_\infty}{1+\omega^2\tau^2}\omega\tau + \frac{\sigma}{\omega\varepsilon_0} \quad (3)$$

where ε_s, ε_∞, σ, ε_0, ω, and τ are the static permittivity, relative permittivity at the high-frequency limit, conductivity, vacuum permittivity, angular frequency, and relaxation time, respectively. The $\varepsilon_c''/\varepsilon_p''$ value reflects the differences in dielectric loss mechanisms [40]. It indicates the predominant role of conduction loss when the value is more than 1. Otherwise, it suggests that polarization loss is the predominant mechanism. The predominant conduction loss is observed in In_2O_{3-x}/C-0 within the S-band and partial C-band, and this phenomenon is primarily attributed to the contribution of electrical conductivity. In contrast, polarization loss dominates in the X-band and Ku-band. With the increase in BIT content, the $\varepsilon_c''/\varepsilon_p''$ value gradually decreases, indicating the enhanced polarization loss, and polarization loss is the predominant mechanism across the 2–18 GHz range.

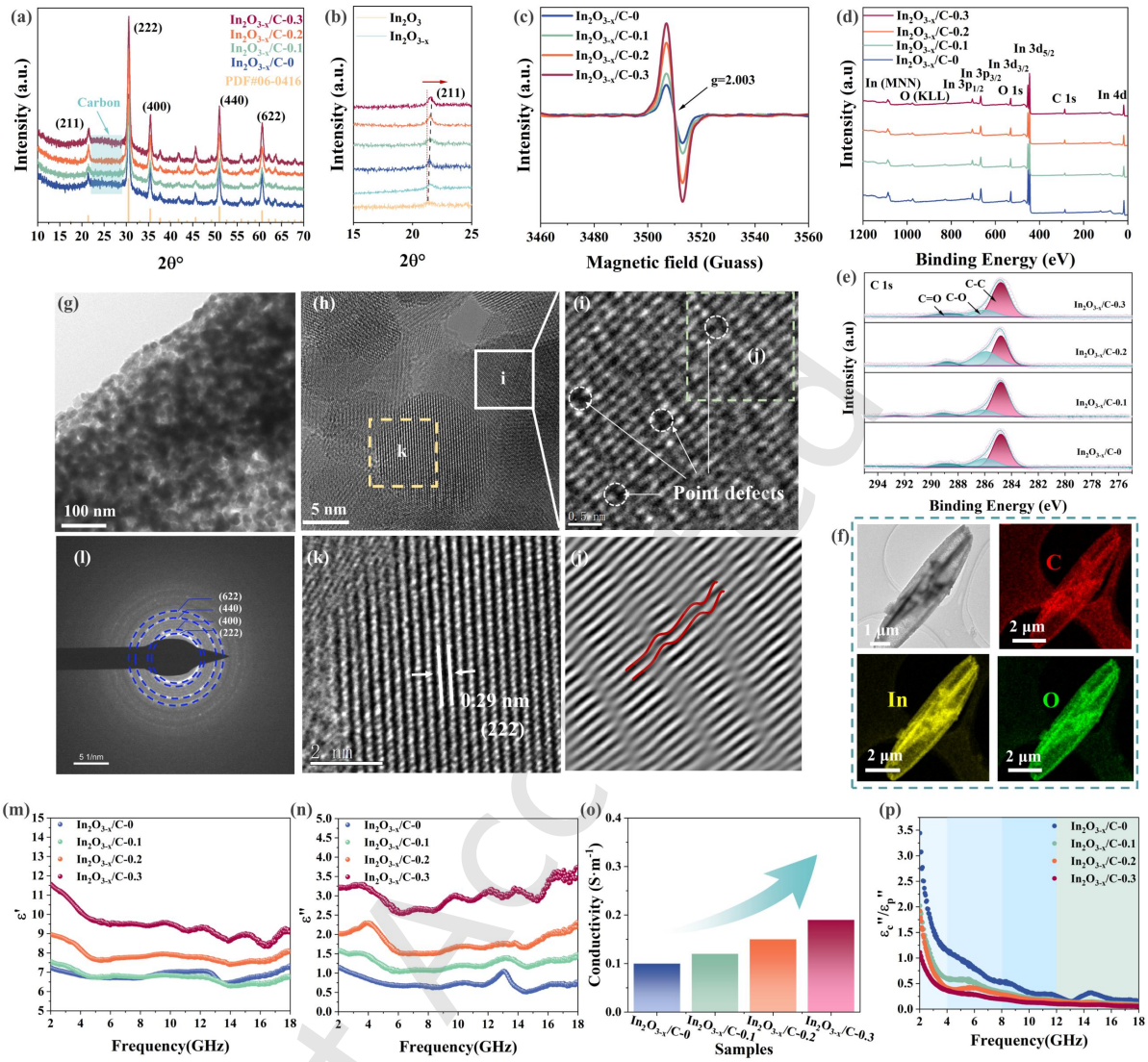

Figure 3 (a) and (b) XRD patterns. (c) EPR spectra. (d) XPS survey spectra of In_2O_{3-x}/C. (e) The C 1s XPS spectrum. (f) TEM image and EDS mapping, (g) and (h) HRTEM images, (i) point defects, (j) lattice distortion, (k) lattice fringe, and (l) SAED pattern of In_2O_{3-x}/C-0.3. (m) Real and (n) imaginary parts of the complex permittivity, (o) conductivity, and (p) conduction-to-polarization loss ratio of In_2O_{3-x}/C.

The 3D *RL* plots of In_2O_{3-x}/C are presented in Figs. 4(a)–4(d). Compared with In_2O_{3-x}, In_2O_{3-x}/C-0 exhibits significantly reduced microwave absorption performance, showing effective absorption only in the high-frequency range and at large thicknesses. Its RL_{min} is -21.72 dB, with an EAB of 1.2 GHz@5.5 mm (16.0–17.2 GHz, Fig. 4(a)). However, the microwave absorption performance progressively improves with increasing BIT dosage. The maximum EABs of In_2O_{3-x}/C-0.1 and In_2O_{3-x}/C-0.2 are 1.9 GHz@5.4 mm (15.8–17.7 GHz, Fig. 4(b)) and 2.9 GHz@1.8 mm (15.1–18.0 GHz, Fig. 4(c)), respectively. Remarkably, In_2O_{3-x}/C-0.3 achieves a RL_{min} of -51.17 dB and a broad EAB of 5.0 GHz@1.9 mm (11.7–16.7

GHz, Fig. 4(d)). The EMW attenuation mechanism of In_2O_{3-x}/C was thoroughly analyzed. Prominent polarization relaxation processes are observable on the Cole-Cole curves (Fig. S9), indicating that polarization loss dominates the attenuation mechanism. These results are consistent with the calculated results presented earlier (Fig. 3(p)). However, the Cole-Cole curve of In_2O_{3-x}/C-0 shows nearly linear behavior in the 2–8 GHz range (Fig. 4(e), e1), suggesting that conduction loss is predominant. As the BIT dosage increases, a larger radius and more semicircles emerge (Fig. 4(e), e2–e4), corresponding to enhanced Debye relaxation processes [41]. Impedance matching is a critical factor influencing the EMW absorption performance of materials. As the normalized impedance matching value ($|Z_{in}/Z_0|$) approaches 1, EMWs can more readily penetrate the material. The introduced BIT improves the impedance matching of In_2O_{3-x}/C-0 (Fig. 4(f)), and In_2O_{3-x}/C-0.3 exhibits $|Z_{in}/Z_0|$ closest to 1, indicating its superior impedance matching to that of the rest samples. Usually, the EMW attenuation capability of materials is characterized by the attenuation coefficient (α). Eq. (4) is used to calculate the α.

$$\alpha = \frac{\sqrt{2}\pi f}{c}\sqrt{(\mu''\varepsilon'' - \mu'\varepsilon') + \sqrt{(\mu''\varepsilon'' - \mu'\varepsilon')^2 + (\mu'\varepsilon'' + \mu''\varepsilon')^2}} \quad (4)$$

As shown in Fig. 4(g), the α of In_2O_{3-x}/C-0.3 is remarkably higher than those of other samples, indicating its superior EMW attenuation capability. The dielectric loss tangent ($\tan\delta_e = \varepsilon''/\varepsilon'$) is used to evaluate the dielectric loss performance of the materials. From Fig. 4(h), the $\tan\delta_e$ curves of all samples closely match their corresponding ε'' curves, confirming that dielectric loss dominates the attenuation mechanism [42]. Moreover, In_2O_{3-x}/C-0.3 shows the highest $\tan\delta_e$ values, indicating that it has the best dielectric loss capability.

The EMW absorption performances of the developed materials are presented in Fig. 4(i). In_2O_3 exhibits almost no response to EMWs (EAB = 0 GHz), whereas In_2O_{3-x} bears significantly enhanced microwave absorption capability (EAB = 3.7 GHz). This remarkable enhancement clearly reflects the effectiveness of oxygen vacancy introduction in improving EMW absorption properties. Meanwhile, mere carbon doping alone fails to yield positive effects, as evidenced by In_2O_{3-x}/C-0 (EAB = 1.2 GHz). The synergistic effect of BIT-induced oxygen vacancies plays a critical role in enhancing the performance of In_2O_{3-x}/C. Furthermore, In_2O_{3-x}/C-0.3 achieves 80% coverage of the Ku-band at a thickness of 1.8 mm and 70% coverage of the X-band at 2.4 mm (Fig. 4(j)), demonstrating its superior bandwidth tunability.

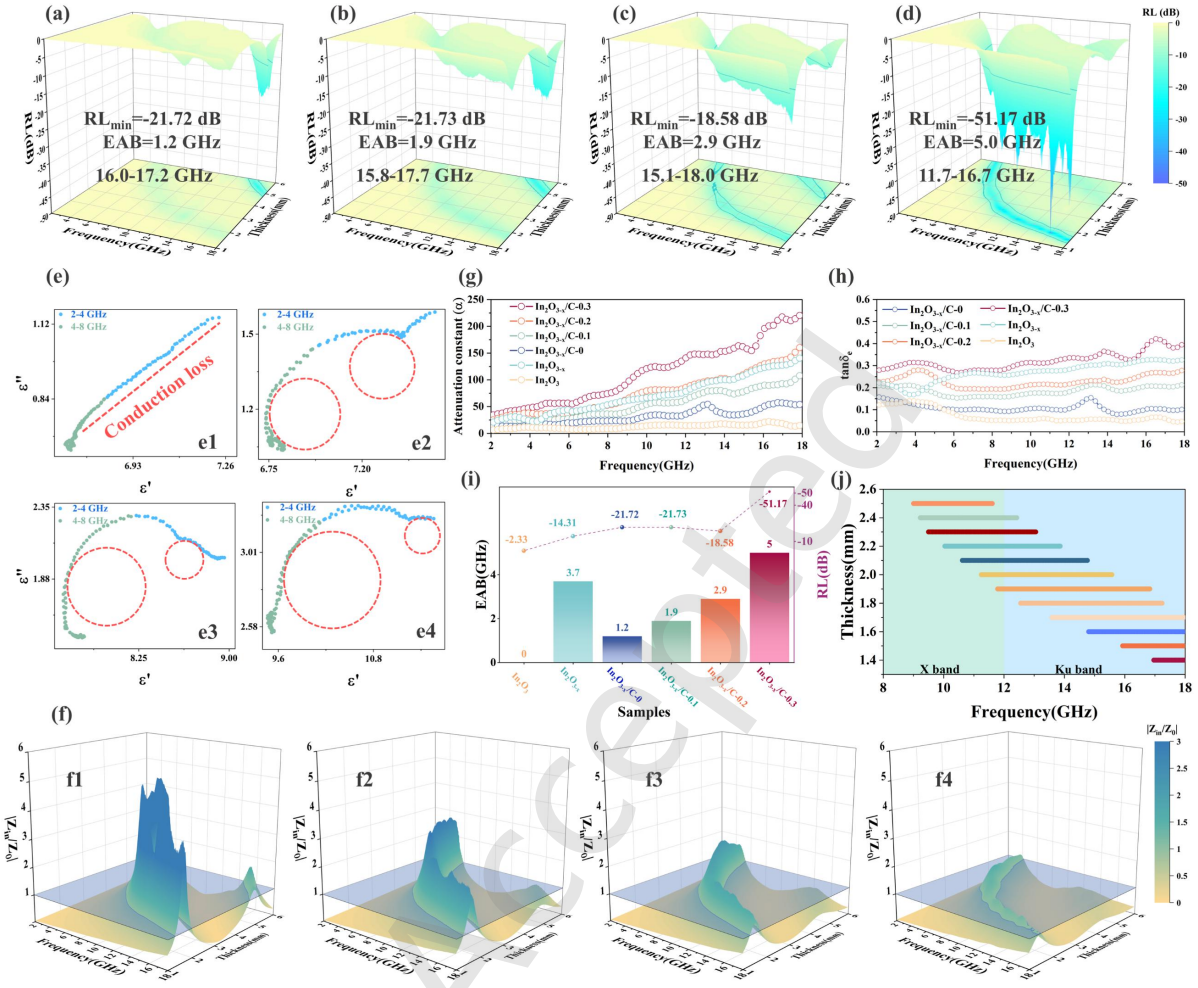

Figure 4 ((a)–(d)) 3D *RL* diagrams of In_2O_{3-x}/C-0, In_2O_{3-x}/C-0.1, In_2O_{3-x}/C-0.2, and In_2O_{3-x}/C-0.3. (e) Cole-Cole curves (e1: In_2O_{3-x}/C-0; e2: In_2O_{3-x}/C-0.1; e3: In_2O_{3-x}/C-0.2; e4: In_2O_{3-x}/C-0.3). (f) 3D impedance matching maps (f1: In_2O_{3-x}/C-0; f2: In_2O_{3-x}/C-0.1; f3: In_2O_{3-x}/C-0.2; f4: In_2O_{3-x}/C-0.3). (g) Attenuation coefficients, (h) dielectric loss tangent, and (i) comparative summary of all samples. (j) EAB of the In_2O_{3-x}/C-0.3 at varying matching thicknesses.

3.4. Analysis of EMW Loss Mechanisms

Density functional theory (DFT) calculations were performed to investigate the electronic band structures of In_2O_3, In_2O_{3-x} and In_2O_{3-x}/C, which assists to elucidate the EMW attenuation mechanism in the In_2O_{3-x} systems. While the pristine In_2O_3 with perfect crystalline structure exhibits a bandgap of 1.133 eV (Fig. 5(a)), the introduction of oxygen vacancies significantly reduces the bandgap to 0.157 eV (Fig. 5(b)). Further carbon doping induces a nearly metallic behavior in In_2O_{3-x}/C, as evidenced by a negligible bandgap of 0.002 eV (Fig. 5(c)). A series of models with different defect concentrations is also constructed (Fig. S10).

The results show that with the increase in defect concentration, the band gap of the system decreases gradually from 1.133 eV in the pristine state to -0.186 eV (Fig. S11). These results validate that the introduction of oxygen vacancies and carbon doping synergistically enhance the electron transition probability. The density of states (DOS) analysis further elucidates the electronic configurations of the materials [43]. Notably, defect states are observed near the Fermi level (E_f) of In_2O_{3-x} (Fig. 5(d)). Furthermore, the increased density of energy levels near the E_f in In_2O_{3-x}/C (Fig. 5(e)) indicates good electrical conductivity [44], which contributes to the material's conduction loss. Fig. 5(f) shows the charge density distribution of In_2O_{3-x}/C with electrons predominantly accumulating at oxygen vacancy sites and electron density decreasing around carbon atoms [45]. The Bader charge analysis is conducted, and the results are highly consistent with those of the 3D and 2D charge density difference analysis, further confirming the significant negative charge (-0.73) accumulation at the oxygen vacancies (Fig. S12). The surrounding electrons' asymmetric redistribution caused by oxygen vacancies and carbon doping can induce the formation of electrical dipoles, thereby promoting the polarization loss [46].

Fig. 5(g) illustrates the EMW absorption mechanisms of In_2O_3 under the influence of oxygen vacancy concentration and carbon doping, which can be summarized as follows: 1) The microwave absorption capability of In_2O_3 highly depends on the oxygen vacancy concentration in the lattice. Introducing oxygen vacancies optimizes the band structure, reduces the bandgap, and enhances electron transition probability, thereby promoting conduction loss. Additionally, oxygen vacancies serve as polarization centers, endowing In_2O_{3-x} with polarization loss capability. Polarization loss dominates the EMW attenuation process. 2) Synergistic effects of oxygen vacancies and carbon doping further reduce the bandgap of In_2O_3 and enhance dielectric loss. However, In_2O_{3-x}/C-0 exhibits significantly degraded EMW absorption. This degradation is attributed to increased oxygen partial pressure as a result of organic decomposition during annealing, which suppresses the formation of oxygen vacancies in the In_2O_3 lattice. The reduced oxygen vacancies weaken the polarization loss, which further causes excessive conduction loss, ultimately leading to impedance mismatch [47]. 3) The BIT incorporation mitigates the effects of organic decomposition, increases oxygen vacancy concentration, and restores polarization loss dominance, thereby

improving impedance matching. Consequently, through the synergy of oxygen vacancies and carbon doping, In_2O_{3-x}/C-0.3 achieves excellent microwave absorption performance.

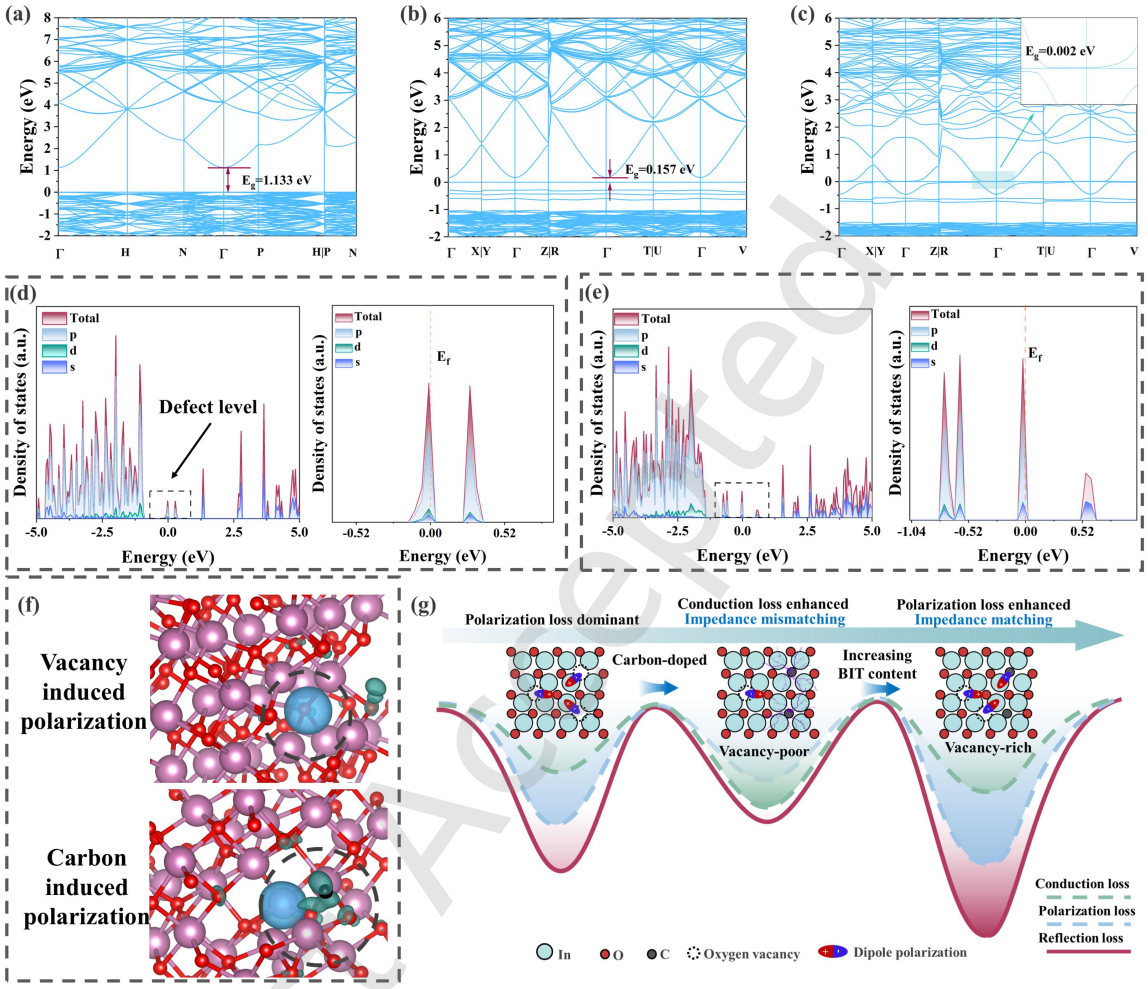

Figure 5 (a) Energy band structure of In_2O_3, (b) In_2O_{3-x}, and (c) In_2O_{3-x}/C. (d) DOSs of In_2O_{3-x} and (e) In_2O_{3-x}/C. (f) Charge density differences of In_2O_{3-x}/C (blue: electron density increases and green: electron density decreases). (g) Schematic diagram of the EMW absorption mechanism for In_2O_{3-x} and In_2O_{3-x}/C.

4. Conclusion

In this study, rod-shaped In_2O_3, In_2O_{3-x}, and In_2O_{3-x}/C particles were synthesized via sequential annealing of the MIL-68(In) precursor under oxygen-rich and vacuum conditions. The effects of oxygen vacancies and carbon doping in the In_2O_3 lattice on the EMW absorption were systematically investigated. The results show that organic decomposition suppresses the generation of oxygen vacancies. However, introducing BIT during precursor preparation mitigates this adverse effect by reducing organic adsorption. The synergistic

enhancement between oxygen vacancies in In_2O_3 and carbon doping significantly improves the microwave absorption capacity. Specifically, oxygen vacancies and carbon doping can reduce the bandgap and increase electron transition probability, thereby enhancing conduction loss. Furthermore, these defects can act as polarization centers to strengthen polarization loss. This work pioneers the use of defect engineering to enhance the electromagnetic response of In_2O_3 in the microwave frequency range, improving the EAB and providing a novel strategy for developing In_2O_3-based EMW absorbers.

Acknowledgments

The authors are thankful for the financial support from the National Natural Science Foundation of China (No. 22375166), Natural Science Basic Research Program of Shaanxi (No. 2024JC-JCQN-44), and Innovation Capability Support Program of Shaanxi Science and Technology

Innovation Team Project (No. 2025RS-CXTD-024).

References

[1] Hou, T.; Jia, Z.; Wang, B.; Li, H.; Liu, X.; Bi, L.; Wu, G. MXene-based accordion 2D hybrid structure with Co_9S_8/C/$Ti_3C_2T_x$ as efficient electromagnetic wave absorber. *Chem. Eng. J.* **2021**, *414*, 128875.

[2] Liu, P.; Gao, S.; Wang, Y.; Huang, Y.; Zhou, F.; Liu, P. Magnetic porous N-doped carbon composites with adjusted composition and porous microstructure for lightweight microwave absorbers. *Carbon* **2021**, *173*, 655-666.

[3] Gao, S.; Zhang, G.; Wang, Y.; Han, X.; Huang, Y.; Liu, P. MOFs derived magnetic porous carbon microspheres constructed by core-shell Ni@C with high-performance microwave absorption. *J. Mater. Sci. Technol.* **2021**, *88*, 56-65.

[4] Huan, X.; Wang, H.; Deng, W.; Yan, J.; Xu, K.; Geng, H.; Guo, X.; Jia, X.; Zhou, J.; Yang, X. Integrating multi-heterointerfaces in a 1D@2D@1D hierarchical structure via autocatalytic pyrolysis for ultra-efficient microwave absorption performance. *Small* **2022**, *18*, 2105411.

[5] Wei, B.; Zhou, C.; Yao, Z.; Chen, P.; Wang, M.; Li, Z.; Zhou, J.; Hou, J.; Li, W. Encapsulation of high specific surface area red blood cell-like mesoporous carbon spheres by magnetic nanoparticles: A new strategy to realize multiple electromagnetic wave loss mechanism. *Carbon* **2021**, *184*, 232-244.

[6] Liu, P.; Gao, S.; Liu, X.; Huang, Y.; He, W.; Li, Y. Rational construction of hierarchical hollow CuS@CoS_2 nanoboxes with heterogeneous interfaces for high-efficiency microwave absorption materials. *Compos. B. Eng.* **2020**, *192*, 107992.

[7] Tariq, M. R.; Ahmad, M.; Naik, M.-u.-d.; Khan, I.; Zhang, B. A comprehensive review of the advancement of transition metal oxide nanocomposites for microwave absorption. *Coord. Chem. Rev.* **2025**, *533*, 216535.

[8] Luo, J.; Wu, L.; Yan, J.; Lv, X.; Luo, Y.; Jiang, W.; Xiong, Z.; Ni, A.; Liu, C.; Che, R. Radar-stealth and thermal-insulating MOF-derived cellulose-carbon aerogels for broadband electromagnetic wave absorption. *Chin. Chem. Lett.* **2025**, *36*, 111065.

[9] Ning, M.; Lei, Z.; Tan, G.; Man, Q.; Li, J.; Li, R. W. Dumbbell-like Fe_3O_4@N-doped carbon@2H/1T-MoS_2 with tailored magnetic and dielectric loss for efficient microwave absorbing. *ACS Appl. Mater. Interfaces* **2021**, *13*, 47061-47071.

[10] He, M.; Zhong, X.; Lu, X.; Hu, J.; Ruan, K.; Guo, H.; Zhang, Y.; Guo, Y.; Gu, J. Excellent low-frequency microwave absorption and high thermal conductivity in polydimethylsiloxane composites endowed by hydrangea-like CoNi@BN heterostructure fillers. *Adv. Mater.* **2024**, *36*, 2410186.

[11] Huang, Z.; Wan, L.; Tian, J.; Sun, Z.; Ahmad, M.; Wu, J.; Zhang, B. NC@TiO_2 microwave-absorber microspheres: control of shell thickness and evaluation of electromagnetic performance. *Carbon* **2025**, *243*, 120511.

[12] Fan, Y.; Zhou, B.; Xing, H.; Zhang, L.; Wu, J.; Zhang, B. Multidimensional Co-design and performance-mechanism study of novel graphdiyne composites with microwave absorbing structures. *Small* **2025**, *21*, 2500132.

[13] Han, Y.; Yang, Y.; Li, T.; Zhang, Y.; Guo, H.; He, M.; Han, K.; Qiu, H.; Gu, J. Hierarchical heterogeneous Co-based magnetic absorbers for superior Broadband high-efficiency microwave absorption. *Adv. Funct. Mater.* **2025**, 10.1002/adfm.202525719, e25719.

[14] Qi, J.; Liang, C.; Ruan, K.; Li, M.; Guo, H.; He, M.; Qiu, H.; Guo, Y.; Gu, J. Cactus-like architecture for synergistic microwave absorption and thermal management. *Natl. Sci. Rev.* **2025**, *12*, nwaf394.

[15] Zhao, J.; Wang, Z.; Wang, H.; Liu, P.; Che, R. Controllable design of "nested doll" MoS_2/V_2O_3 heterostructures promotes polarization effects for high-efficiency microwave absorption. *Adv. Funct. Mater.* **2024**, *35*, 2418282.

[16] Zeng, B.; Zhang, F.; Zhao, K.; Ahmad, M.; Wu, J.; Zhang, L.; Lan, D.; Zhang, B. Multilayered heterostructures and multicomponent synergy in MnO@HsGDY@NC/Ni magnetic nanofibers for enhanced electromagnetic wave absorption. *J. Mater. Sci. Technol.* **2026**, *251*, 193-202.

[17] Fang, G.; Liu, C.; Xu, M.; Zhang, X.; Wu, Y.; Kim, D. H.; Ji, G. The elaborate design of multi-polarization effect by non-edge defect strategy for ultra-broad microwave absorption. *Adv. Funct. Mater.* **2024**, *34*, 2404532.

[18] Liang, J.; Ye, F.; Cao, Y.; Mo, R.; Cheng, L.; Song, Q. Defect-engineered graphene/Si_3N_4 multilayer alternating core-shell nanowire membrane: a plainified hybrid for broadband electromagnetic wave absorption. *Adv. Funct. Mater.* **2022**, *32*, 2200141.

[19] Vu, N. T. T.; Loh, L.; Chen, Y.; Wu, Q.; Verzhbitskiy, I. A.; Watanabe, K.; Taniguchi, T.; Bosman, M.; Ang, Y. S.; Ang, L. K.; Trushin, M.; Eda, G. Single atomic defect conductivity for selective dilute impurity imaging in 2D semiconductors. *ACS Nano* **2023**, *17*, 15648-15655.

[20] Liu, J.; Zhang, L.; Wu, H. Anion-doping-induced vacancy engineering of cobalt sulfoselenide for boosting electromagnetic wave absorption. *Adv. Funct. Mater.* **2022**, *32*, 2200544.

[21] Liu, Y.; Zhou, X.; Jia, Z.; Wu, H.; Wu, G. Oxygen vacancy-induced dielectric polarization prevails in the electromagnetic wave-absorbing mechanism for Mn-based MOFs-derived composites. *Adv. Funct. Mater.* **2022**, *32*, 2204499.

[22] Zhang, B.; Jing, Q.; Yan, S.; Guo, J.; Liu, W.; Sun, C.; Wang, Z. Electron irradiation modified point defects of SiC nanoparticles with tunable high electromagnetic wave absorption. *Carbon* **2024**, *218*, 118727.

[23] Liu, L.; He, C.-C.; Zeng, J.; Peng, Y.-H.; Chen, W.-Y.; Zhao, Y.-J.; Yang, X.-B.

Theoretical study of oxygen-vacancy distribution in In_2O_3. *J. Phys. Chem. C* **2021**, *125*, 7077-7085.

[24] Buckeridge, J.; Catlow, C. R. A.; Farrow, M. R.; Logsdail, A. J.; Scanlon, D. O.; Keal, T. W.; Sherwood, P.; Woodley, S. M.; Sokol, A. A.; Walsh, A. Deep vs shallow nature of oxygen vacancies and consequent n-type carrier concentrations in transparent conducting oxides. *Phys. Rev. Mater.* **2018**, *2*, 054604.

[25] Chatratin, I.; Sabino, F. P.; Reunchan, P.; Limpijumnong, S.; Varley, J. B.; Van de Walle, C. G.; Janotti, A. Role of point defects in the electrical and optical properties of In_2O_3. *Phys. Rev. Mater.* **2019**, *3*, 074604.

[26] Sun, L.; Li, R.; Zhan, W.; Yuan, Y.; Wang, X.; Han, X.; Zhao, Y. Double-shelled hollow rods assembled from nitrogen/sulfur-codoped carbon coated indium oxide nanoparticles as excellent photocatalysts. *Nat. Commun.* **2019**, *10*, 2270.

[27] Perdew, J. P.; Ernzerhof, M.; Burke, K. Rationale for mixing exact exchange with density functional approximations. *J. Chem. Phys.* **1996**, *105*, 9982-9985.

[28] McRoberts, K.; Zhou, W. Reversed crystal growth of metal organic framework MIL-68(In). *CrystEngComm* **2021**, *23*, 7658-7662.

[29] Ohya, Y.; Yamamoto, T.; Ban, T. Equilibrium dependence of the conductivity of pure and Tin-doped indium oxide on oxygen partial pressure and formation of an intrinsic defect cluster. *J. Am. Ceram. Soc.* **2007**, *91*, 240-245.

[30] Wang, Q.; Chen, Y.; Liu, X.; Li, L.; Du, L.; Tian, G. Sulfur doped In_2O_3-CeO_2 hollow hexagonal prisms with carbon coating for efficient photocatalytic CO_2 reduction. *Chem. Eng. J.* **2021**, *421*, 129968.

[31] Han, L.; Jing, F.; zhang, J.; Luo, X.-Z.; Zhong, Y.-L.; Wang, K.; Zang, S.-H.; Teng, D.-H.; Liu, Y.; Chen, J.; Yang, C.; Zhou, Y.-T. Environment friendly and remarkably efficient photocatalytic hydrogen evolution based on metal organic framework derived hexagonal/cubic In_2O_3 phase-junction. *Appl. Catal. B Environ.* **2021**, *282*, 119602.

[32] Cheng, Q.; Huang, M.; Xiao, L.; Mou, S.; Zhao, X.; Xie, Y.; Jiang, G.; Jiang, X.; Dong, F. Unraveling the influence of oxygen vacancy concentration on electrocatalytic CO_2 reduction to formate over indium oxide catalysts. *ACS Catal.* **2023**, *13*, 4021-4029.

[33] Wei, W.; Wei, Z.; Li, R.; Li, Z.; Shi, R.; Ouyang, S.; Qi, Y.; Philips, D. L.; Yuan, H.

Subsurface oxygen defects electronically interacting with active sites on In_2O_3 for enhanced photothermocatalytic CO_2 reduction. *Nat. Commun.* **2022**, *13*, 3199.

[34] Qiu, C.; Sun, J.; Li, M.; Mao, C.; Song, R.; Zhang, Z.; Perovic, D. D.; Howe, J. Y.; Wang, L.; Ozin, G. A. Irreversible lattice expansion effects in nanoscale indium oxide for CO_2 hydrogenation catalysis. *J. Am. Chem. Soc.* **2024**, *146*, 33997-34007.

[35] Wang, Z.; Meng, X.; Guo, Q.; Su, C.; Deng, G.; Liu, H.; Yao, Z.; Zhang, S.; Liu, H.; Hao, H. Formation and evolution of oxygen vacancy layer in $BaTiO_3$ dielectric ceramics under thermal and electric field stimuli. *Acta Mater.* **2025**, *299*, 121450.

[36] Xu, F. F.; Cai, B.; Sun, X. B.; Zhang, Y.; Bai, S.; Liang, C. M.; Koo, M. C.; Bai, Y. X.; Zhao, P. Y.; Wang, G. S. A strategy for modulation of permittivity in manganese doping to induce lattice distortion. *InfoMat.* **2026**, *8*, e70087.

[37] Tariq, M. R.; Ge, F.; Ahmad, M.; Zhang, B. Ramie plant-derived low-cost multi-phase HPCFs@n-$MoSe_2$ (n = 2H, 2H/1T and 1T) multilayered flower-like structures for wideband electromagnetic wave absorption applications. *Carbon* **2026**, *246*, 120924.

[38] Lin, J.; Peng, Y.; Luo, J.; Xiong, Z.; Huang, J.; Zeng, X.; Wu, L.; Peng, J.; Liu, C. One-click to 3D: helical carbon nanotube-mediated MXene hierarchical aerogel with layer spacing engineering for broadband electromagnetic wave absorption. *Small Methods* **2025**, *9*, e2401665.

[39] Ágoston, P.; Erhart, P.; Klein, A.; Albe, K. Geometry, electronic structure and thermodynamic stability of intrinsic point defects in indium oxide. *J. Phys.:Condens. Matter* **2009**, *21*, 455801.

[40] Xiao, J.; Zhan, B.; He, M.; Qi, X.; Zhang, Y.; Guo, H.; Qu, Y.; Zhong, W.; Gu, J. Mechanically robust and thermal insulating nanofiber elastomer for hydrophobic, corrosion-resistant, and flexible multifunctional electromagnetic wave absorbers. *Adv. Funct. Mater.* **2025**, *35*, 2419266.

[41] Jiang, Q.; Xu, L.; Tang, Z.; Xie, C.; Lu, J.; Han, Z.; Zhang, D.; Zuo, C. A competitive strategy toward 1 T/2H MoS_2 to balance impedance for optimizing electromagnetic wave absorption. *Chem. Eng. J.* **2024**, *491*, 151854.

[42] Jia, Z.; Liu, J.; Gao, Z.; Zhang, C.; Wu, G. Molecular intercalation-induced two-phase evolution engineering of 1T and 2H-MS_2(M = Mo, V, W) for

interface-polarization-enhanced electromagnetic absorbers. *Adv. Funct. Mater.* **2024**, *35*, 2405523.

[43] Xing, H.; Ge, F.; Cheng, H.; Kou, Q.; Wu, J.; Zhang, B. Fractal topology directed 3D conductive metal–organic frameworks: coordination mode regulation and multiscale electromagnetic wave absorption mechanisms. *Adv. Funct. Mater.* **2025**, 10.1002/adfm.202522523, e22523.

[44] Yao, K.; Pan, F.; Liang, H.; Zhang, X.; Li, L.; Song, L.; Yang, Y.; Yuan, B.; Lu, W. Shifting d-band center: an overlooked factor in broadening electromagnetic wave absorption bandwidth. *Adv. Funct. Mater.* **2024**, *35*, 2413639.

[45] Lin, J.; Wen, H.; Feng, Z.; Hu, R.; Wu, L.; Liu, C.; Lin, S.; Peng, Y.; Liu, Y.; Che, R. Anion injection in dielectric ecosystems to construct dual built-in electric fields for efficient electromagnetic response. *Adv. Funct. Mater.* **2025**, *35*, 2505381.

[46] Zhang, X.; Li, B.; Xu, J.; Zhang, X.; Shi, Y.; Zhu, C.; Zhang, X.; Chen, Y. Metal ions confined in periodic pores of MOFs to embed single-metal atoms within hierarchically porous carbon nanoflowers for high-performance electromagnetic wave absorption. *Adv. Funct. Mater.* **2022**, *33*, 2210456.

[47] Xu, L.; Tao, J.; Zhang, X.; Yao, Z.; Wei, B.; Yang, F.; Zhou, C.; Zavabeti, A.; Zuraiqi, K.; Zhou, J. Hollow C@MoS_2 nanospheres for microwave absorption. *ACS Appl. Nano Mater.* **2021**, *4*, 11199-11209.

Electronic Supplementary Material

Oxygen vacancies regulation of In_2O_3 for enhancing microwave absorption by conduction and polarization loss balance

Boli Zeng[1,2,§], Haowen Xing[1,§], Yihao Fan[1], Jianfeng Wu[1,3], Feijie Ge[1,*], Shuanmei Li[4], Baoliang Zhang[1,3,*]

[1] School of Chemistry and Chemical Engineering, Northwestern Polytechnical University, Xi'an 710129, China

[2] Xi'an Key Laboratory of Functional Organic Porous Materials, Northwestern Polytechnical University, Xi'an 710072, China

[3] Shaanxi Engineering and Research Center for Functional Polymers on Adsorption and Separation, Sunresins New Materials Co. Ltd., Xi'an 710072, China

[4] Northwest Rubber & Plastics Research and Design Institute Co., Ltd., Xi'an 712023, China

[§] Boli Zeng and Haowen Xing contributed equally to this work.

Address correspondence to Feijie Ge, feijie.ge@nwpu.edu.cn; Baoliang Zhang, blzhang@nwpu.edu.cn

Supporting information to https://doi.org/10.26599/NR.2026.94908746

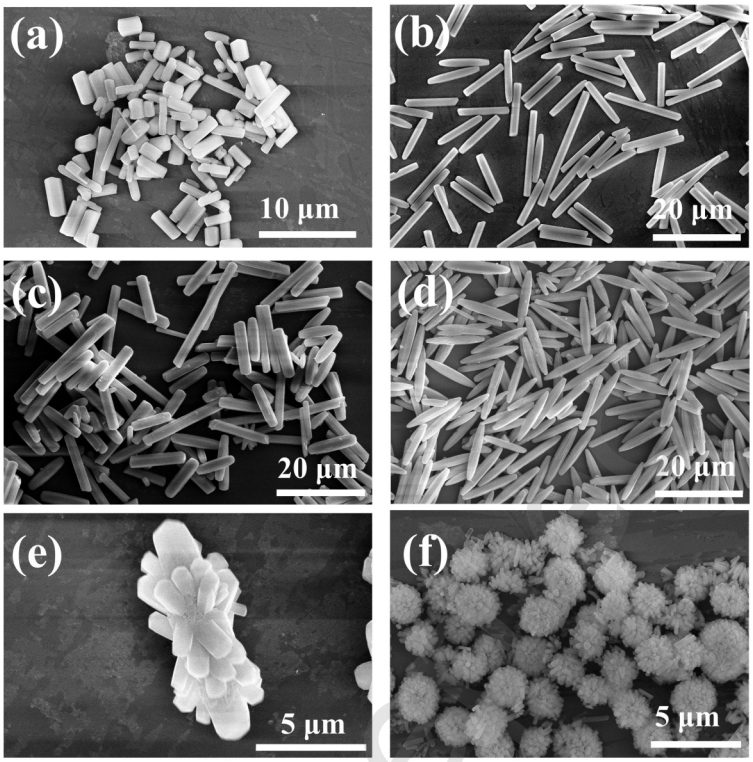

Figure S1 SEM images of MIL-68(In) series. (a) MIL-0, (b) MIL-0.1, (c) MIL-0.2, (d) MIL-0.3, (e) MIL-0.4 and (f) MIL-0.5.

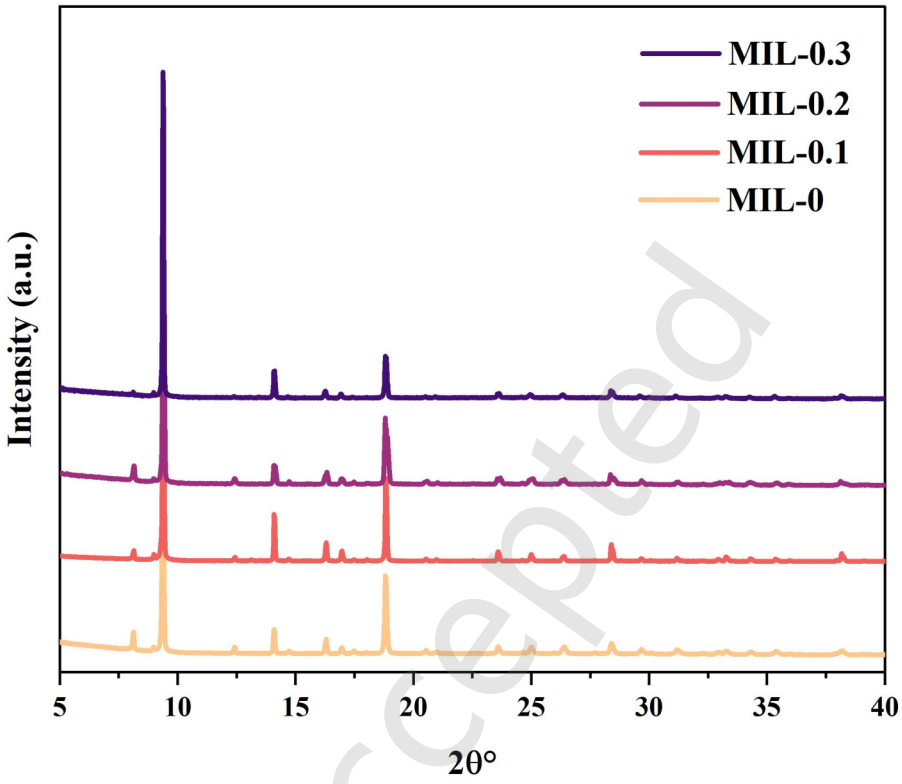

Figure S2 XRD patterns of MIL-68(In) series.

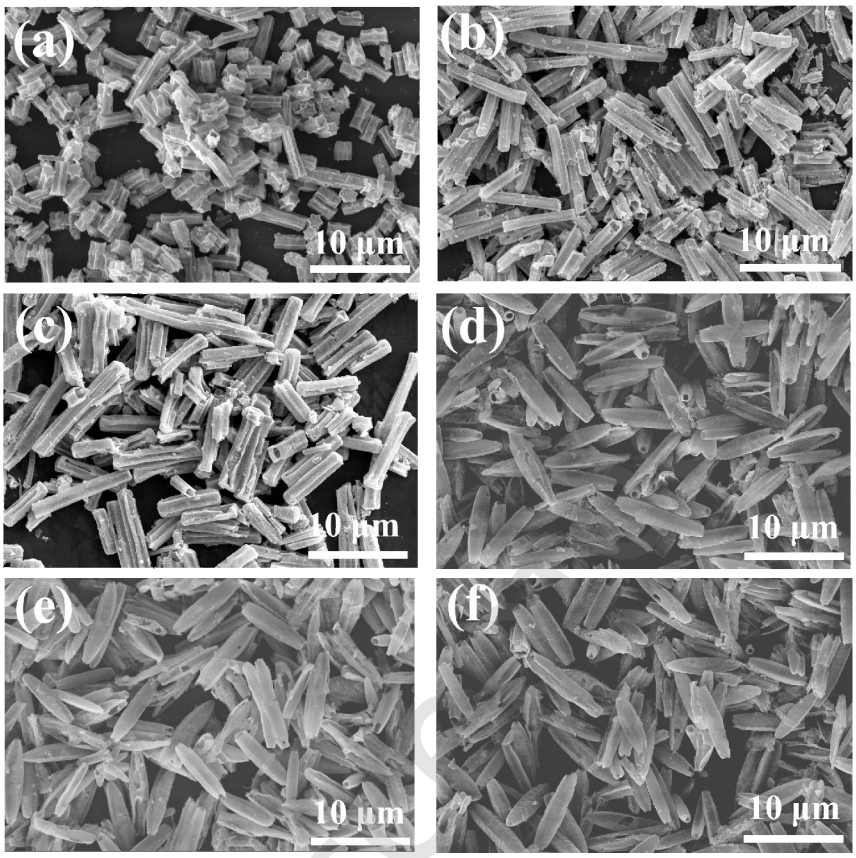

Figure S3 SEM images of In_2O_3, In_2O_{3-x} and In_2O_{3-x}/C series. (a) In_2O_{3-x}/C-0, (b) In_2O_{3-x}/C-0.1, (c) In_2O_{3-x}/C-0.2, (d) In_2O_{3-x}/C-0.3, (e) In_2O_3 and (f) In_2O_{3-x}.

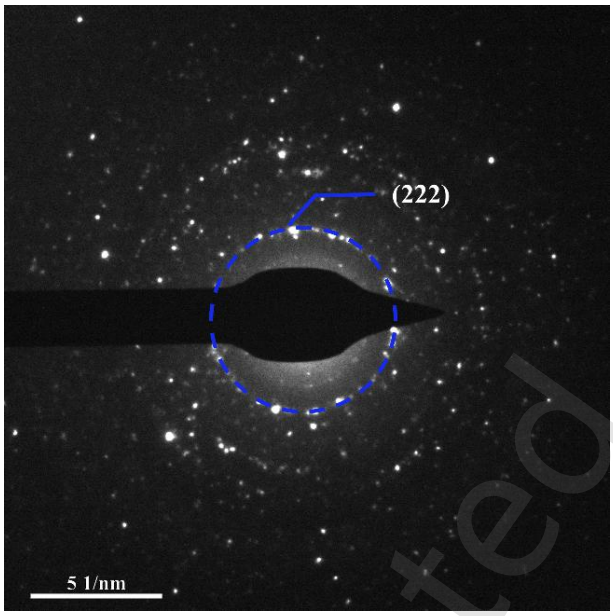

Figure S4 SAED image of In_2O_{3-x}.

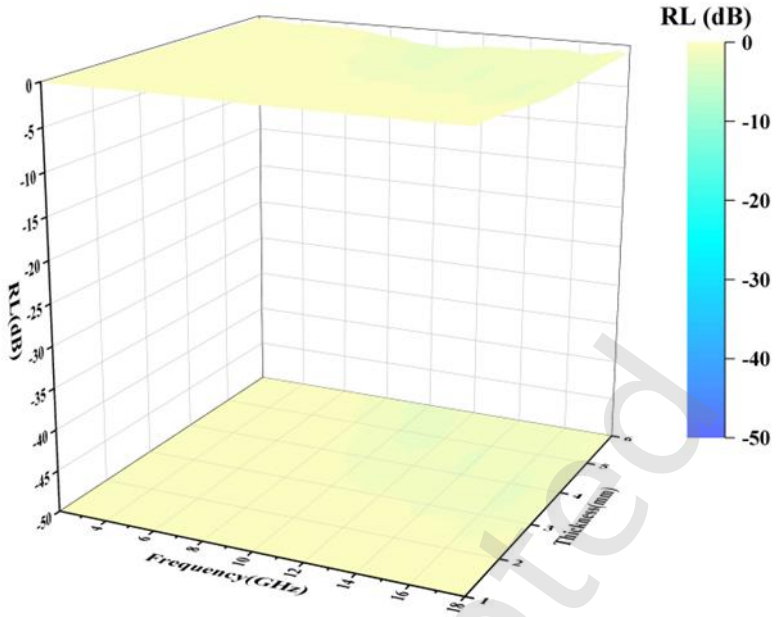

Figure S5 The 3D *RL* map of In_2O_3.

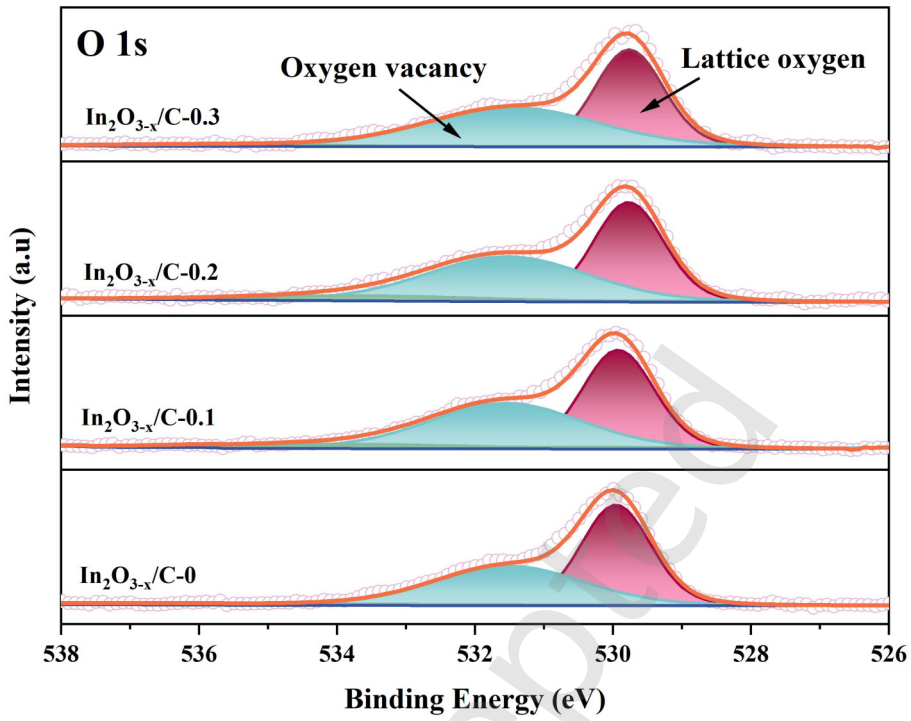

Figure S6 XPS spectra of O 1s.

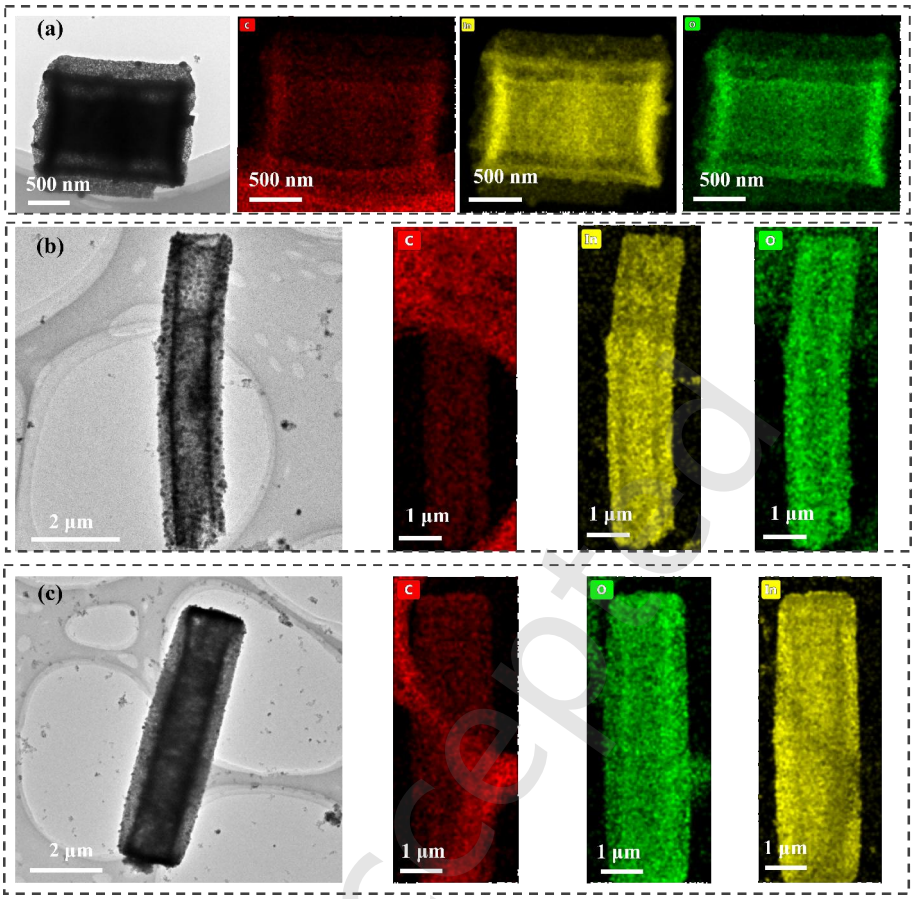

Figure S7 TEM images and EDS mapping of (a) In_2O_{3-x}/C-0, (b) In_2O_{3-x}/C-0.1 and (c) In_2O_{3-x}/C-0.2.

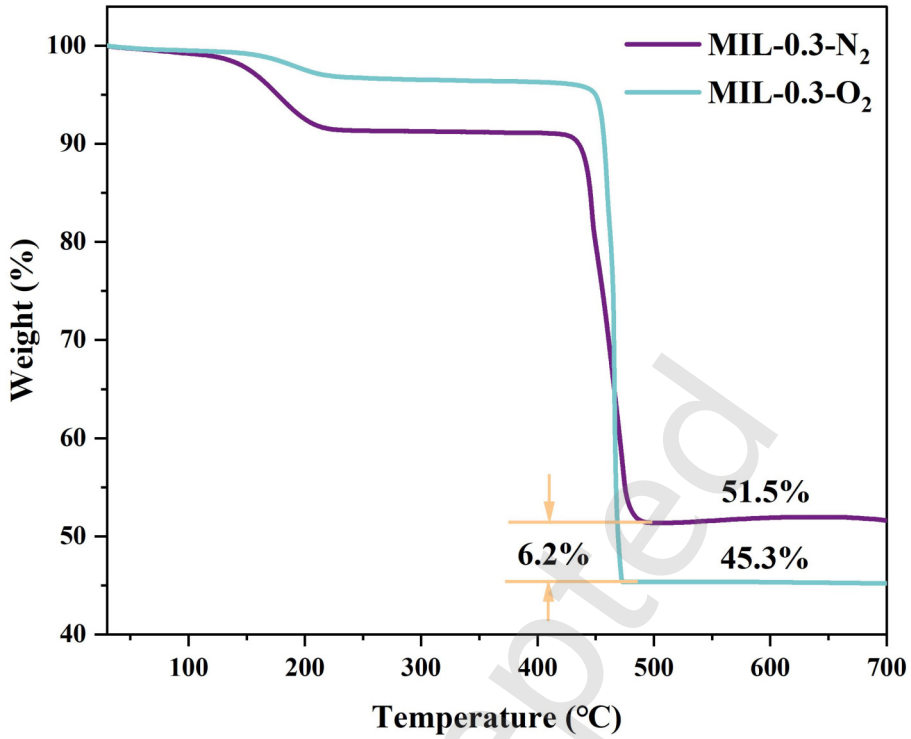

Figure S8 TG curves of MIL-0.3 at N_2 and O_2 atmosphere.

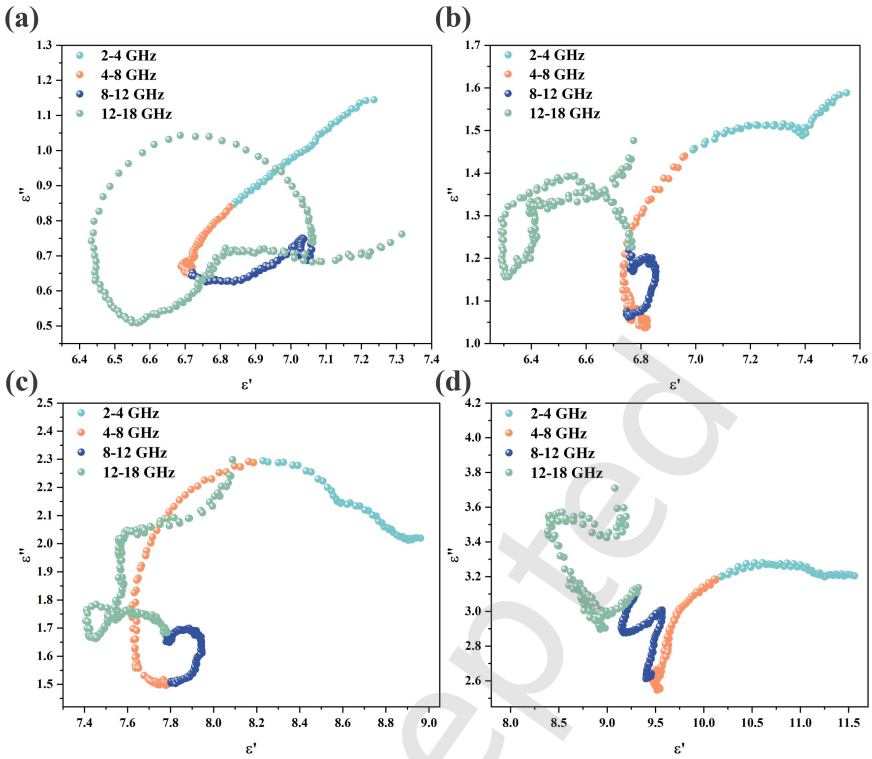

Figure S9 Cole-Cole curves of (a) In_2O_{3-x}/C-0, (b) In_2O_{3-x}/C-0.1, (c) In_2O_{3-x}/C-0.2 and (d) In_2O_{3-x}/C-0.3.

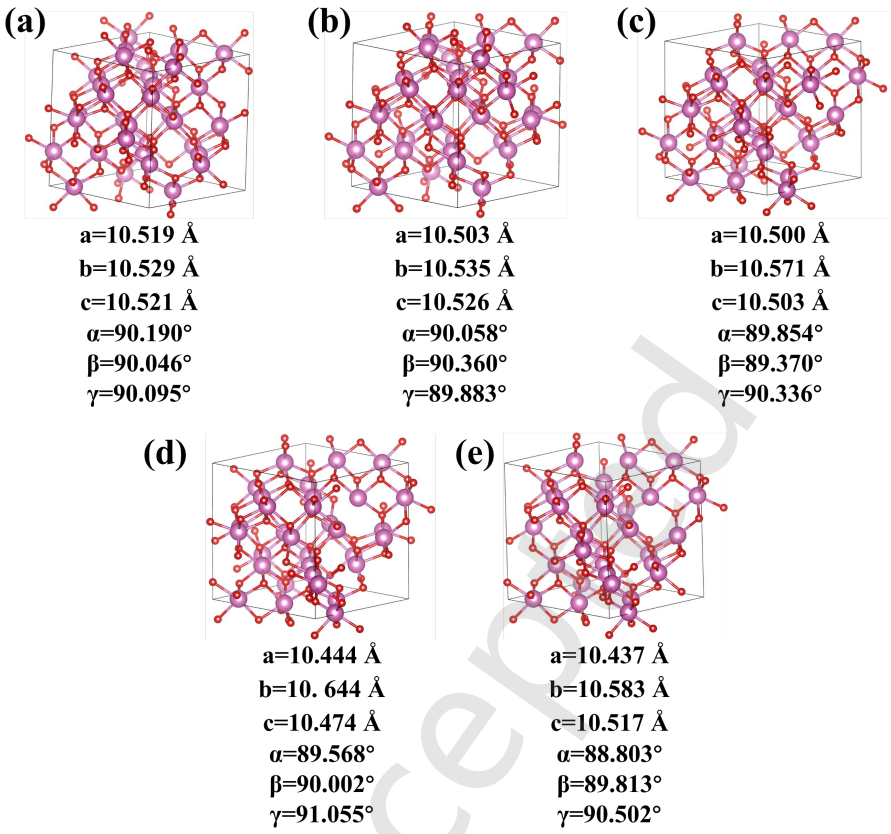

Figure S10 Crystal model of In_2O_{3-x} with defect concentration of (a) 1.25%, (b) 2.50%, (c) 3.75%, (d) 5.00%, and (e) 6.25%.

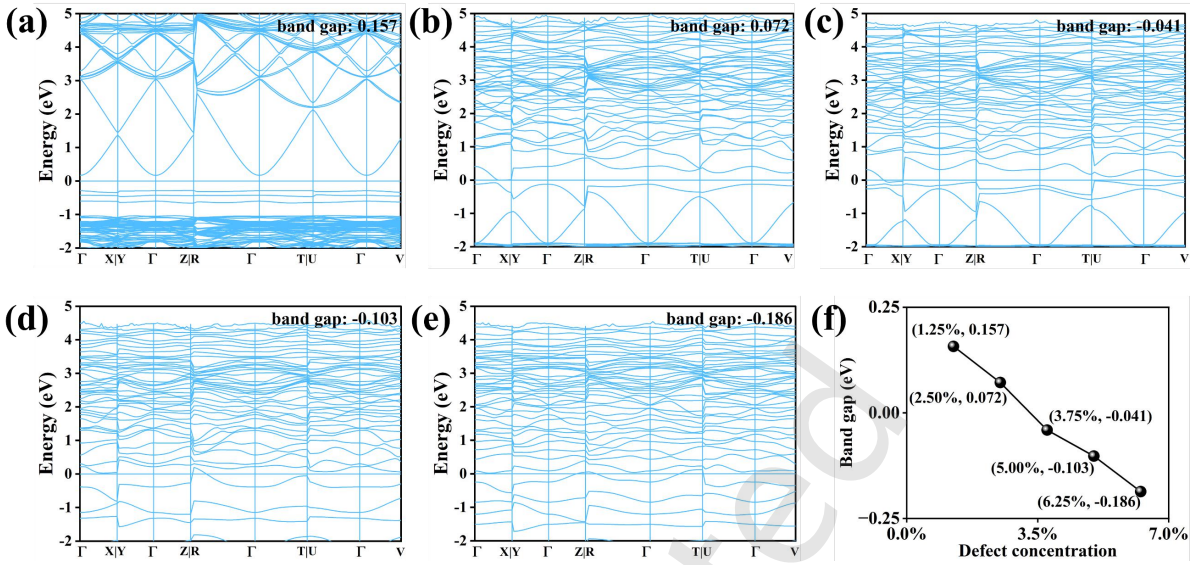

Figure S11 Energy band structure of In_2O_{3-x} with defect concentration of (a) 1.25%, (b) 2.50%, (c) 3.75%, (d) 5.00%, and (e) 6.25%. (f) The variation of band gap with defect concentration.

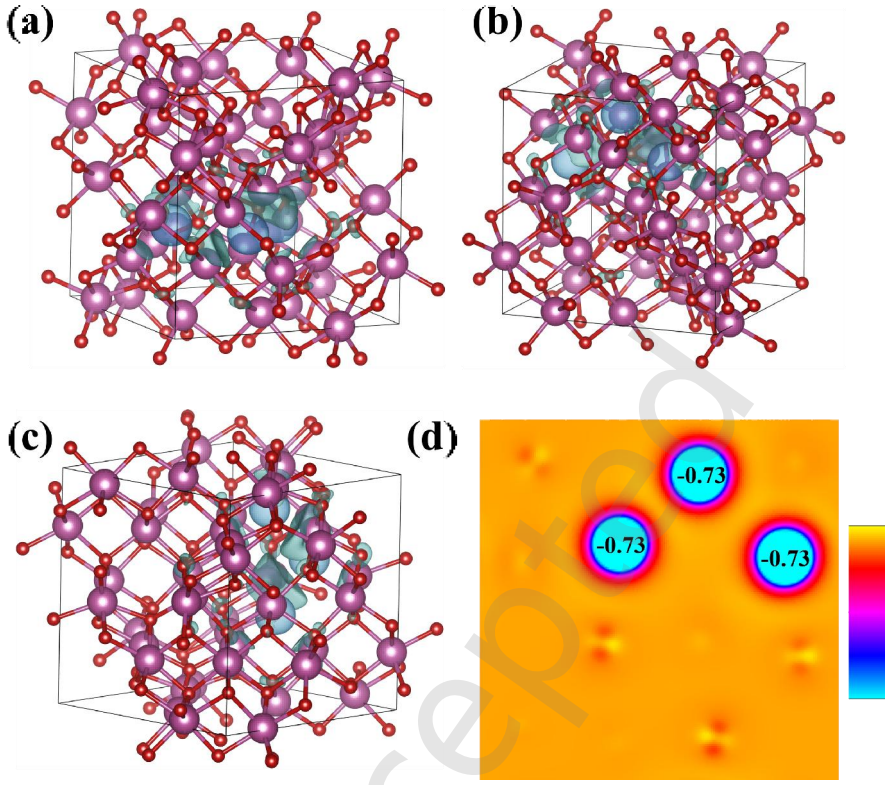

Figure S12 Charge density difference cross-section of In_2O_{3-x} in the direction of (a) x, (b) y and (c) z. (d) Bader charge analysis of In_2O_{3-x}.